Large-scale dynamics of the mesosphere and lower thermosphere: an analysis using the extended Canadian Middle Atmosphere Model

Large-scale dynamics of the mesosphere and lower thermosphere: An analysis using the extended Canadian Middle Atmosphere Model

C. McLandress,[1] W. E. Ward,[2] V. I. Fomichev,[3] K. Semeniuk,[3] S. R. Beagley,[3] N. A. McFarlane,[4] and T. G. Shepherd[1]

Received 18 October 2005; revised 27 February 2006; accepted 10 May 2006; published 14 September 2006.

[1] The extended Canadian Middle Atmosphere Model is used to investigate the large-scale dynamics of the mesosphere and lower thermosphere (MLT). It is shown that the 4-day wave is substantially amplified in southern polar winter in the presence of instabilities arising from strong vertical shears in the MLT zonal mean zonal winds brought about by parameterized nonorographic gravity wave drag. A weaker 4-day wave in northern polar winter is attributed to the weaker wind shears that result from weaker parameterized wave drag. The 2-day wave also exhibits a strong dependence on zonal wind shears, in agreement with previous modeling studies. In the equatorial upper mesosphere, the migrating diurnal tide provides most of the resolved westward wave forcing, which varies semiannually in conjunction with the tide itself; resolved forcing by eastward traveling disturbances is dominated by smaller scales. Nonmigrating tides and other planetary-scale waves play only a minor role in the zonal mean zonal momentum budget in the tropics at these heights. Resolved waves are shown to play a significant role in the zonal mean meridional momentum budget in the MLT, impacting significantly on gradient wind balance. Balance fails at low latitudes as a result of a strong Reynolds stress associated with the migrating diurnal tide, an effect which is most pronounced at equinox when the tide is strongest. Resolved and parameterized waves account for most of the imbalance at higher latitudes in summer. This results in the gradient wind underestimating the actual eastward wind reversal by up to 40%.

Citation: McLandress, C., W. E. Ward, V. I. Fomichev, K. Semeniuk, S. R. Beagley, N. A. McFarlane, and T. G. Shepherd (2006), Large-scale dynamics of the mesosphere and lower thermosphere: An analysis using the extended Canadian Middle Atmosphere Model, *J. Geophys. Res.*, *111*, D17111, doi:10.1029/2005JD006776.

1. Introduction

[2] The past decade has seen the development of a number of comprehensive general circulation models (GCMs) extending upward from the Earth's surface to 120 km and higher [e.g., *Miyahara et al.*, 1993; *Norton and Thuburn*, 1999; *Fomichev et al.*, 2002; *Richter and Garcia*, 2006; *Schmidt et al.*, 2006]. The motivation for building such models has been the growing awareness of the role of the mesosphere and lower thermosphere (MLT) as a possible indicator of climate change, and the availability of global wind and temperature data sets against which the models can be compared. Being a dynamically complex region, characterized by a rich spectrum of waves forced mainly in the troposphere but also in situ by instabilities, the MLT poses a significant challenge for middle atmosphere models. In contrast to mechanistic models that have lower boundaries near the tropopause, GCMs generate tropospheric waves internally and so are the only models truly capable of testing, in a self-consistent manner, our understanding of the dynamical processes affecting the middle atmosphere.

[3] The UK Universities' Global Atmospheric Modelling Programme (UGAMP) GCM was used by *Norton and Thuburn* [1996, 1999] to investigate the role of parameterized nonorographic gravity wave drag (GWD) in generating the 2-day wave, a prominent planetary-scale disturbance in the middle atmosphere during solstice [e.g., *Wu et al.*, 1993]. Those results showed that the parameterized GWD was crucial in creating and maintaining the shears in the summer mesosphere zonal mean zonal winds that were responsible for generating a realistic 2-day wave in the model.

[4] The extended Canadian Middle Atmosphere Model (CMAM) [*Fomichev et al.*, 2002] was used by *McLandress* [2002a, 2002b] to investigate the causes of the observed semiannual variation of the migrating diurnal tide in the equatorial MLT [e.g., *Hays et al.*, 1994; *McLandress et al.*,

[1]Department of Physics, University of Toronto, Toronto, Ontario, Canada.
[2]Department of Physics, University of New Brunswick, Fredericton, New Brunswick, Canada.
[3]Department of Earth and Space Science and Engineering, York University, Toronto, Ontario, Canada.
[4]Stratospheric Processes and Their Role in Climate International Project Office, Department of Physics, University of Toronto, Toronto, Ontario, Canada.

0148-0227/06/2005JD006776

1996]. Those studies demonstrated that the seasonal variation of the tide, which was well reproduced in the model, resulted from a combination of solar and latent heating in the troposphere and meridional gradients in the background winds in the middle atmosphere.

[5] Observations suggest that the migrating diurnal tide also plays an important role in the zonal mean zonal momentum budget in the equatorial MLT, providing forcing of up to −20 m/s/day near 95 km [*Lieberman and Hays*, 1994]. Mechanistic modeling studies have shown that momentum deposition by the tide generates equatorial easterlies in the lower thermosphere, as well as cell-like structures in the meridional circulation [*Miyahara*, 1978]. These features have been borne out by the Middle Atmosphere Circulation Model at Kyushu University (MACMKU) [*Miyahara et al.*, 1993]. The role of other large-scale waves, however, is unclear. Recent work by *Richter and Garcia* [2006] using the Whole Atmosphere Community Climate Model (WACCM) suggests that the 2-day wave may provide significant forcing of the westerly phase of the mesospheric semiannual oscillation during solstice.

[6] GCMs have also been used to evaluate gradient wind balance in the MLT. This is an important issue since zonal winds are generally derived from satellite temperatures using the gradient wind approximation [e.g., *Fleming and Chandra*, 1989; *Garcia and Clancy*, 1990], the validity of which is questionable in the MLT where wave driving is significant. Motivated by the observational study of *Lieberman* [1999a], which showed that the gradient wind approximation failed in the equatorial MLT (possibly as a result of tidal aliasing in the satellite data), *Miyahara et al.* [2000] used the MACMKU to show that the breakdown of gradient balance at low latitudes resulted from the Reynolds stress associated with resolved disturbances in the model. They went on to suggest that the migrating diurnal tide was responsible, but did not demonstrate this explicitly. Since their simulation considered only perpetual equinox conditions and did not include the effects of parameterized GWD, the applicability of their results to other seasons and latitudes is unknown.

[7] In this paper the extended CMAM is used to examine a number of dynamical processes related to the issues raised above. This study is a follow-on to that of *Fomichev et al.* [2002, hereinafter referred to as F02], which documented the model and examined the general features of the simulated zonal mean circulation and energy budget. Here, the analysis is extended to include a detailed investigation of the resolved wave driving in the zonal mean zonal and meridional momentum equations. It is important to note that this is a process study, focused on understanding the physical mechanisms in the model which are responsible for generating these waves and their impact on the zonal mean circulation. Although qualitative comparisons to observations are made, this study is not intended as a model validation.

[8] This paper also explores the forcing mechanisms of the 4-day wave, a ubiquitous planetary-scale disturbance in the Southern Hemisphere winter stratosphere [e.g., *Venne and Stanford*, 1982] that is also observed in the MLT [*Fraser et al.*, 1993; *Lawrence et al.*, 1995; *Palo et al.*, 1998], but which has received little attention in GCMs. (To our knowledge the only study is that of *Norton and Thuburn* [1997] using a version of the UGAMP model with a lid at 95 km, which focused on the 4-day wave in the stratosphere.) Previous analyses have suggested that the 4-day wave is generated at mesospheric heights by barotropic instability of the zonal mean zonal winds [*Manney*, 1991; *Randel and Lait*, 1991; *Lawrence and Randel*, 1996]. This inference was based on the existence of a "double-jet" structure in the COSPAR International Reference Atmosphere (CIRA) [*Fleming et al.*, 1990] zonal mean zonal winds in Southern Hemisphere winter, characterized by a westerly jet maximum in the subtropics near 60 km and a secondary maximum at higher latitudes. It is not known how frequently this double-jet structure occurs, or whether it extends into the lower thermosphere where the 4-day wave is observed. As will be demonstrated, vertical shears in the zonal mean zonal winds, which are brought about by parameterized nonorographic GWD, play an important role in generating the CMAM 4-day wave in the MLT as a result of baroclinic instability.

[9] The paper is organized as follows. Section 2 briefly describes the extended CMAM. This section also includes a general discussion of the sensitivity of GCM simulations to both the GWD and convective parameterizations, since these are physical processes that impact strongly on the MLT, but which have aspects that are poorly constrained by observations. Section 3 describes the model simulations and the diagnostics used in this study. The model results are discussed in the next three sections: Section 4 describes the general features of the zonal mean circulation. Section 5 focuses on the dominant planetary-scale waves in the MLT that are forcing the zonal mean zonal winds. These include the 2-day wave, 4-day wave, and equatorial waves. Section 6 examines wave forcing of the zonal mean meridional momentum equation, and in particular gradient wind balance. We conclude with a summary and brief discussion.

2. Model Description

[10] The extended Canadian Middle Atmosphere Model is based on the standard version of the CMAM described by *Beagley et al.* [1997]. It employs a T32 spectral truncation with 70 levels in the vertical that extend from the ground to 2×10^{-7} hPa (∼210 km in geopotential height), which corresponds to a horizontal resolution of ∼6° and a vertical resolution of ∼3 km in the middle atmosphere. This resolution is adequate to resolve the vertically propagating migrating diurnal tide in the MLT region, which is dominated by the (1,1) Hough mode component, as verified using the linear tidal model described in *McLandress* [2002b]. Parameterizations of most of the important physical processes from the surface to the lower thermosphere are included. Those pertaining to the upper atmosphere are described in F02; they include nonlocal thermodynamic equilibrium infrared cooling, extreme ultraviolet solar heating, nonorographic GWD, ion drag, and molecular diffusion. Since the model simulates only the neutral atmosphere (i.e., no ionized gases or auroral effects), the region above about 120 km is primarily considered as a deep viscous layer for dissipating upward propagating waves that would otherwise be affected by the upper boundary if the standard version of the model were used. The present version of the model does not have interactive chemistry. In addition, it should be noted that the boundary conditions and external forcings used in this configuration of the model (e.g., prescribed sea surface temperatures and solar flux) have no year-to-year variations.

[11] A nonorographic GWD parameterization is an important component of current middle atmosphere GCMs, which is used to bring about the mesospheric zonal mean zonal wind reversals and also to provide additional wave forcing for the quasi-biennial and mesospheric semiannual oscillations in the tropics. In the extended CMAM the Doppler-spread parameterization of *Hines* [1997a, 1997b] is used. The gravity wave source spectrum is specified near the surface and is horizontally isotropic in intrinsic phase speed and constant in space and time. These settings, as well as the others listed in F02, produce the general features of the observed zonal mean zonal winds as shown in that paper. In addition to GWD, the vertical eddy diffusivity and heating which are produced by the Hines parameterization are also employed.

[12] While it is not expected that the response to dynamical or radiative forcings will be strongly dependent on the type of dissipation mechanism used in nonorographic GWD parameterizations [*McLandress and Scinocca*, 2005], a strong dependence on the gravity wave source spectrum used in the parameterizations most certainly occurs. Since observations of gravity waves in the lower atmosphere are insufficient to constrain the parameterizations, modelers choose a source spectrum that produces extratropical mean winds that resemble the observations. However, careful tuning of the sources to produce realistic zonal mean zonal winds does not mean that the actual source spectrum has been found since the nature of the inverse problem does not guarantee a unique answer. The philosophy here is to use simple source settings unless compelled otherwise by observations or theory.

[13] A tropospheric convective parameterization is another component of a GCM that has a strong impact on the middle atmosphere through the generation of waves by latent heating. *Horinouchi et al.* [2003] have shown that different convective parameterizations produce very different spectra of upward propagating equatorial waves. In the CMAM the deep convective parameterization of *Zhang and McFarlane* [1995] is used. This parameterization produces a latent heating spectrum that peaks strongly at low frequencies, the diurnal frequency, and the harmonics of the diurnal frequency (i.e., semidiurnal, terdiurnal, etc.), but has less power at other frequencies. Recent work by *Scinocca and McFarlane* [2004] indicates that the *Zhang and McFarlane* [1995] scheme can produce a realistic amount of temporal variability of precipitation (and hence of vertically averaged latent heating) for horizontal resolutions that are typically employed in middle atmosphere GCMs like the CMAM. For the parameter settings used here, however, the total variance may be somewhat underestimated. The reasons for this are discussed in *Scinocca and McFarlane* [2004].

3. Model Simulations and Diagnostics

[14] Results from two model simulations are presented. The first is for the last 2 years of the 3-year simulation with nonorographic GWD that is discussed in F02; this will be referred to as the control simulation. The second is for the last year of a 4-year simulation without nonorographic GWD, which is otherwise identical to the first. Because of the prescribed sea surface temperatures, solar flux, and parameterized gravity wave source spectrum discussed above, the model does not exhibit much interannual variability outside the polar winter stratosphere. Consequently, the conclusions we draw are not impacted by the relatively short duration of these simulations.

[15] Model diagnostics are computed from instantaneous winds and temperatures that have been saved at 3-hour intervals. Since CMAM energy spectra have very little power at periods shorter than ~3 hours [*Manson et al.*, 2002], this saving interval is sufficient to capture the bulk of the wave variance. Tendencies from the physical parameterizations are computed a posteriori, using the 3-hour archived winds and temperatures as input.

[16] Resolved wave driving is computed using the Eliassen-Palm (EP) flux divergence given by *Andrews et al.* [1987]. To ensure that the numerical formulation did not introduce significant finite-difference errors, the wave driving was also computed in a different but analytically identical manner consistent with the model numerics. This was done by using the exact form of the nonlinear advection terms used in the CMAM, instead of the flux form used in the transformed Eulerian mean zonal wind equation given by *Andrews et al.* [1987]. The resulting differences were found to be small. All results that are shown are computed using the flux form.

[17] Zonal wavenumber and frequency spectra are computed from the 3-hour archived data using a discrete Fourier transform, as in *Horinouchi et al.* [2003]. Time windows of 20 and 60 days are used, with the former being advanced by 10 days and the latter being centered at midmonth. The ends of the time series are tapered beforehand. Monthly mean migrating diurnal tides are also computed from the archived data using the method described by *McLandress* [2002a].

[18] All heights are log-pressure, computed using a scale height of 7 km. True height and log-pressure height differ by no more than a few kilometers in the mesosphere, but start to deviate substantially in the thermosphere where temperature increases rapidly with height. Note that the model lid is located at ~150 km in log-pressure height and ~210 km in geopotential height. F02 used geopotential height in presenting their results.

4. Zonal Mean Circulation

[19] Figure 1 shows the zonal mean zonal and meridional winds for the control simulation for June, July, and August (JJA) and March, April, and May (MAM). (Although results are plotted up to the model lid for completeness, the focus is on the region below about 120 km where the model physics are most representative.) The impact of the parameterized nonorographic GWD is most readily seen in JJA where the zonal wind exhibits reversals in the extratropical upper mesosphere. The reversal is more pronounced in the summer hemisphere, in agreement with the zonal mean zonal winds compiled for the UARS (Upper Atmosphere Research Satellite) Reference Atmosphere Project (URAP) [*Swinbank and Ortland*, 2003]. While the structure of the zonal wind is in qualitative agreement with both the URAP and CIRA climatologies, the summer mesospheric easterlies are too strong and the winter hemisphere westerly jet does not exhibit the equatorward tilt or the double-jet structure. The strong simulated easterlies are a consequence of the simplified source settings used for the Hines GWD parameterization as discussed in section 2.

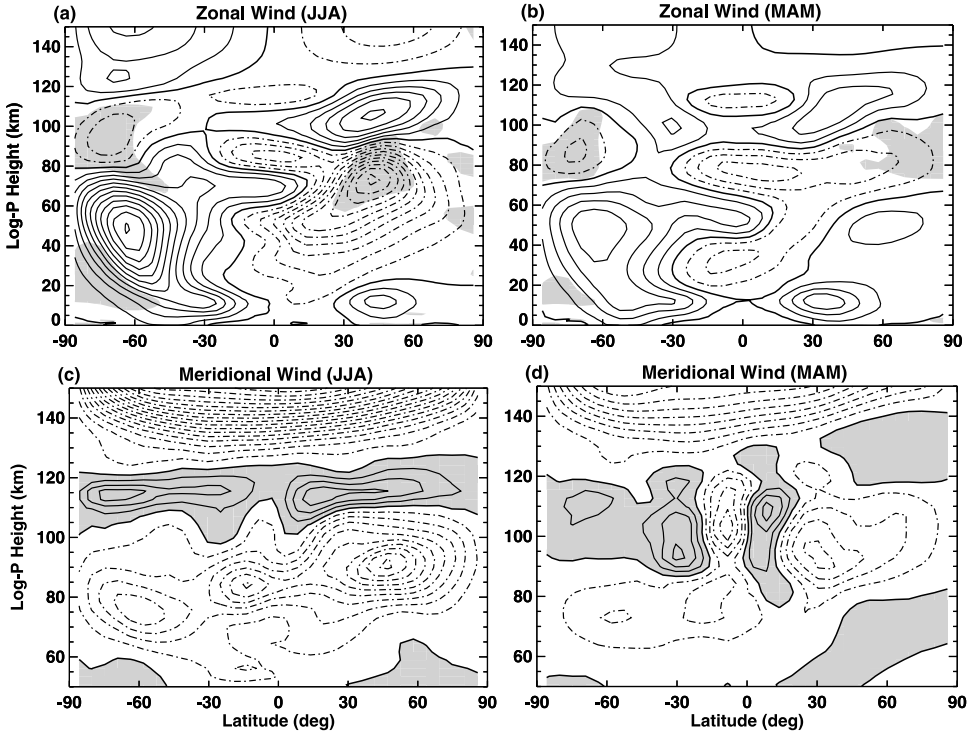

Figure 1. (a and b) Zonal mean zonal and (c and d) meridional winds for June, July, and August (Figures 1a and 1c) and March, April, and May (Figures 1b and 1d) for the control simulation. Shading in Figures 1a and 1b denotes regions where the latitudinal gradient of zonal mean PV is negative. Contour intervals of 10 and 2 m/s are used in the Figures 1a and 1b and Figures 1c and 1d, respectively. The zero contours are thick; negative values are dashed. Two-year averages are shown. Note that the range of plotted heights differs.

[20] The shading in Figures 1a and 1b denotes regions where the latitudinal gradient of Ertel potential vorticity (PV) is negative, and so is an indication of possible wave generation through baroclinic or barotropic instabilities [see *Andrews et al.*, 1987, p. 250]. (PV is computed from monthly and zonal mean zonal winds and temperatures.) Two such regions occur in the upper mesosphere in JJA: in the Northern Hemisphere (NH) easterlies and above the Southern Hemisphere (SH) westerlies. A third region is seen in the SH lower stratosphere on the poleward side of the westerlies.

[21] The meridional wind for JJA (Figure 1c) is characterized by southward (summer-to-winter) flow in the mesosphere. This thermally indirect circulation is primarily driven by the nonorographic GWD and is strongest in the summer upper mesosphere where the GWD is strongest (see Figure 10c of F02). The meridional wind reversal between 100 and 120 km is a direct result of resolved wave drag, as explained below. Above 120 km, where molecular diffusion and ion drag begin to dominate, the flow reverts to southward and increases in speed up to the model lid. In this viscously dominated region the circulation is thermally direct as discussed in F02.

[22] The meridional wind for MAM (Figure 1d) exhibits a distinct cell-like structure at low latitudes between 90 and 120 km, with speeds of up to 8 m/s. This is a consequence of momentum deposition by the migrating diurnal tide, whose amplitude is largest near the equinoxes in the model [*McLandress*, 2002a]. This cell-like structure, which is in good agreement with the GCM results of *Miyahara et al.* [1993], is probably too weak to be seen in satellite data as a result of tidal aliasing.

[23] Figures 2a and 2b show the EP flux divergence per unit mass (i.e., $\nabla \cdot \vec{F}/(\rho_o\, a \cos\phi)$ henceforth referred to as EPFD) for the control simulation for the solstice and equinox seasons. (EPFD is the right-hand-side forcing term in the zonal mean zonal momentum equation in the transformed Eulerian mean formulation given by *Andrews et al.* [1987]. The quantities ρ_o, a, and ϕ used in defining EPFD are, respectively, the reference density in log-pressure coordinates, the Earth's radius and latitude.) The two regions of negative PV gradients (shaded) in JJA near 40°N and 70°S at 80 km coincide with positive regions of EPFD. As will be discussed in detail in sections 5.1 and 5.2, these are the regions where the 2-day and 4-day waves are generated. The wave forcing in MAM (Figure 2b) is substantially weaker than in JJA. This is in correspondence with the weaker wind shears in the upper mesosphere in MAM (Figure 1b).

[24] Figure 2c shows the EPFD computed using only zonal wavenumbers 1 to 4 for JJA. As can be seen by comparison with Figure 2a, the region of positive EPFD below about 100 km in the SH is produced mainly by planetary scales, while that in the NH is due largely to higher wavenumbers. The planetary-scale contribution to resolved wave forcing in MAM (Figure 2d) is dominated by negative EPFD at low latitudes between 80 and 120 km. This forcing, as well as the negative forcing above 140 km that is also seen in JJA, is mainly due to the migrating diurnal tide, as confirmed by a separate calculation using only the tidal winds and temper-

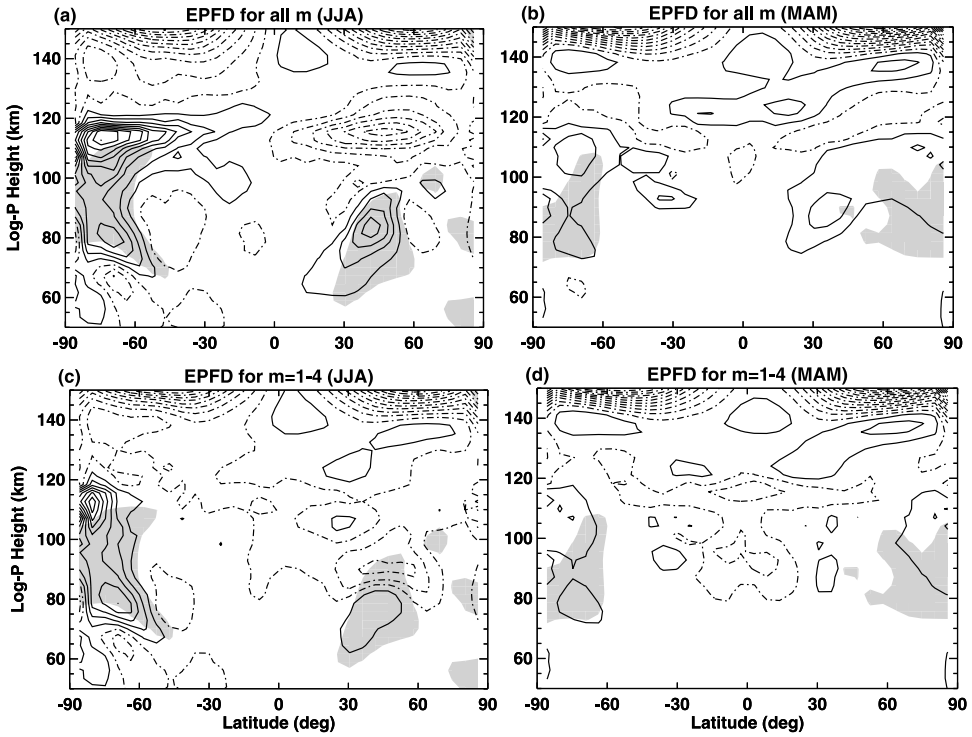

Figure 2. $\nabla \cdot \vec{F}/(\rho_o\, a \cos\phi)$ computed using all zonal wavenumbers (a and b) m and (c and d) $m = 1-4$ for June, July, and August (Figures 2a and 2c) and March, April, and May (Figures 2b and 2d) for the control simulation. Shading denotes regions where the latitudinal gradient of zonal mean PV is negative. Contours are staggered about zero using an interval of 10 m/s/day (i.e., ±5, ±15, . . .); negative values are dashed. Two-year averages are shown.

ature (not shown). In addition to the migrating tide, the waves that make up the resolved wave forcing in the equatorial MLT include nonmigrating tides, the 2-day wave, Kelvin waves, and inertia gravity waves. These will be discussed in section 5.3.

[25] The two regions of oppositely signed EPFD between 110 and 120 km in Figure 2a (i.e., positive in the SH and negative in the NH) are due almost entirely to zonal wavenumbers >4. This drag is approximately balanced by the Coriolis force, indicating that the narrow region of northward flow seen in Figure 1c is generated by this resolved wave drag. The presence of this drag layer is possibly due to the horizontal diffusion in the model, which rapidly increases with height above about 110 km (see F02). While the narrowness of the drag layer may be somewhat artificial, the drag itself is not, since it would occur higher up as a result of molecular diffusion if the enhanced horizontal diffusion was not present. Since the results presented in the subsequent sections focus primarily on the upper mesosphere, the impact of the enhanced horizontal diffusion is unimportant.

[26] Figure 3 shows results for JJA for the simulation without parameterized nonorographic GWD. As expected, there are no zonal wind reversals in the upper mesosphere. The absence of the reversal in SH winter has also stabilized the polar MLT, as seen by the lack of both the negative PV gradients and the positive EPFD that are seen in the control simulation (Figure 2). The negative PV gradients in NH summer are less localized and extend to the pole; this is associated with a more spatially diffuse region of EPFD of positive sign from about 60 to 120 km. Without nonorographic GWD the meridional winds in the mesosphere are also much weaker. The meridional wind maxima near 95 km in the NH and also near 120 km in the SH, therefore, occur in response to the resolved wave drag. Note also the absence of the narrow region of northward flow between 110 and 120 km that was seen in Figure 1b. This is most likely a consequence of the weaker zonal mean zonal wind shears, which produce fewer high-wavenumber disturbances as seen by comparing Figures 2 and 3.

5. Planetary Wave Driving

[27] This section examines the dominant planetary-scale waves in the model and discusses their impact on the zonal mean zonal momentum budget. This includes the 2-day and 4-day waves, which are generated in situ in the upper mesosphere during the solstice months, and equatorial waves, which are generated mainly in the troposphere and propagate up to the MLT. Regarding the 2-day and 4-day waves, where the importance of parameterized nonorographic GWD is demonstrated, results from both model simulations are discussed. The section on equatorial waves focuses primarily on the control simulation.

5.1. Two-Day Wave

[28] Figure 4 shows the zonal wavenumber (m) and frequency (ω) spectrum of EPFD for JJA averaged over northern midlatitudes in the upper mesosphere for the control simulation. The sharp spectral peak at (westward) $m = -3$

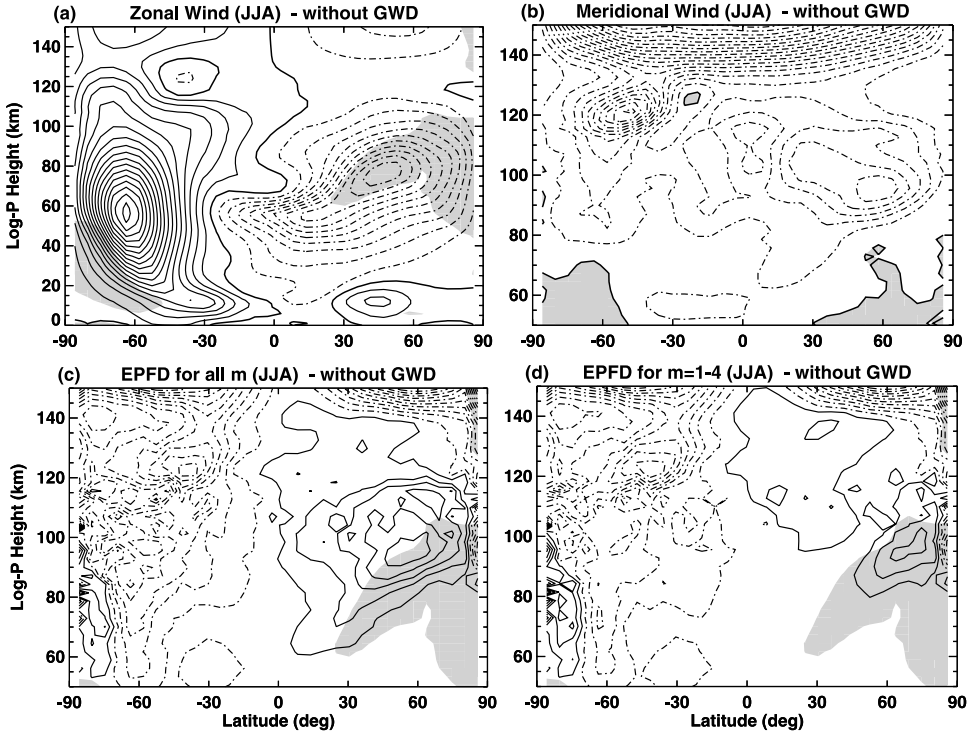

Figure 3. (a and b) Zonal mean zonal and meridional winds for June, July, and August for the 1-year simulation without nonorographic GWD and (c and d) the corresponding $\nabla \cdot \vec{F}/(\rho_o\, a \cos\phi)$ computed using all zonal wavenumbers m and $m = 1-4$. Shading in Figures 3a, 3c, and 3d denotes regions where the latitudinal gradient of zonal mean PV is negative. Contour intervals of 10 and 2 m/s are used in Figures 3a and 3b, respectively; zero wind lines are thick. Contours in Figures 3c and 3d are staggered about zero using an interval of 10 m/s/day (i.e., ±5, ±15, ...). Negative values are dashed in all panels. Note that the range of plotted heights differs.

and $\omega \sim 0.6$ cycles per day (cpd) is the 2-day wave. The frequency is somewhat higher than the observed ~0.5 cpd, presumably as a result of differences in the mesospheric easterlies (Figure 1a), which are stronger than observed.

[29] The amplitude and phase of the meridional wind component of the 2-day wave are shown in Figure 5a for a 20-day period in late July/early August when the wave is strongest. The amplitude maximizes at about 40 m/s in the summer hemisphere near 100 km and extends well into the winter hemisphere. The phase lines indicate a westward tilt of the wave with increasing height above 70 km. These results agree well with the observed spatial structure of the 2-day wave, which has maximum meridional winds of about 40 m/s at midlatitudes in the summer hemisphere at 90 km [*Limpasuvan et al.*, 2005]. The corresponding temperature amplitude from the CMAM (not shown) peaks at about 10 K near 90 km and 40°N, also in good agreement with the observations [*Limpasuvan et al.*, 2005].

[30] The latitude-height structure of the simulated 2-day wave in January (not shown) is similar to that in July, but with a maximum amplitude that is a factor of two weaker. This in contrast to the observations which indicate large wave amplitudes in both months [e.g., *Wu et al.*, 1993; *Riggin et al.*, 2004]. Possible reasons for the weak amplitude in January in the simulation are discussed at the end of this subsection.

[31] The 2-day wave EP flux divergence ($\nabla \cdot \vec{F}$) and EP flux vectors ($\vec{F}$) are shown in Figure 5b for the 20-day period in July/August. The vertically stacked regions of $\nabla \cdot \vec{F}$, with positive values coinciding with negative PV gradients, are characteristic of baroclinic instability. Since the zonal mean temperature in the mesosphere (see Figure 3a of F02) is decreasing toward the cold summer pole, the upward EP flux above 70 km corresponds to a downgradient (poleward) meridional heat flux. Note also that the wave amplitude maximum occurs well above the region of instability near 65 km.

[32] The 2-day wave EP flux vectors (Figure 5b) and corresponding EPFD (not shown) are in good agreement with the observational estimates of *Lieberman* [1999b, 2002], which show that the EPFD is dominated by the vertical convergence of the meridional heat flux, indicating that baroclinic instability is generating the wave. Moreover, the maximum value of the EPFD (−50 m/s/day), found near 90 km at midlatitudes, agrees well with the CMAM results (−80 m/s/day).

[33] The instability that generates the 2-day wave can be described using the quasi-geostrophic form of the inviscid wave activity equation [*Andrews et al.*, 1987]:

$$\frac{\partial A}{\partial t} + \nabla \cdot \vec{F} = 0 \qquad (1)$$

where $A \equiv \frac{1}{2}\rho_0 \overline{q'^2}/\bar{q}_y$ is the wave activity, $\frac{1}{2}\overline{q'^2}$ is the wave enstrophy, and $\bar{q}_y$ is the latitudinal gradient of the zonal mean quasi-geostrophic PV. In the region where $\nabla \cdot \vec{F} > 0$

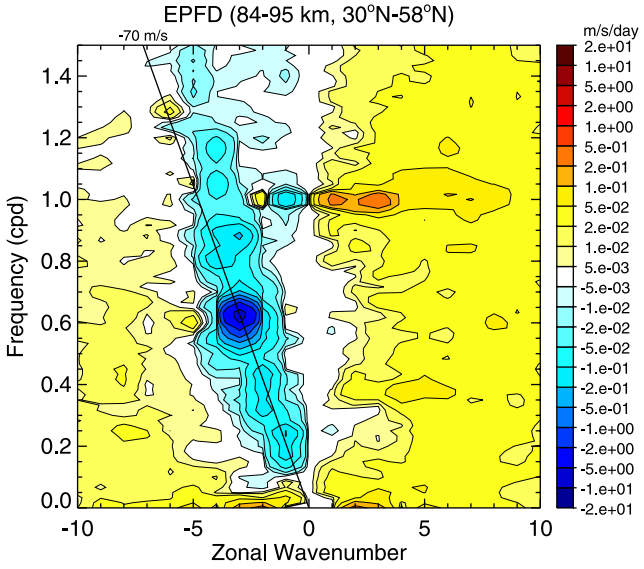

Figure 4. Zonal wavenumber (m) and frequency (ω) spectrum of $\nabla \cdot \vec{F}/(\rho_o\, a \cos\phi)$ averaged from 30°N to 58°N and from 84 to 95 km for June, July, and August for the control simulation. Positive and negative values of m denote eastward and westward traveling disturbances, respectively. The spectral peak at $m = -3$ and $\omega \sim 0.6$ cpd is the 2-day wave. A 1:2:1 smoother has been applied once in the ω direction. The straight line denotes a line of constant phase speed, computed at the midpoint of the latitude band. Latitudinal averaging is area weighted. Results for each month are computed using a 60-day window. A 2-year average is shown.

and $\bar{q}_y < 0$ in Figure 5b, negative wave activity is increasing with time. Likewise, in the adjacent regions where $\nabla \cdot \vec{F} < 0$ and $\bar{q}_y > 0$, positive wave activity is increasing with time. The net result is a disturbance with zero total wave activity whose amplitude is growing in time. (In an equilibrated state, i.e., $\partial A/\partial t = 0$, $\nabla \cdot \vec{F}$ is balanced by dissipation. Nevertheless, $\nabla \cdot \vec{F}$ will take the opposite sign to $\bar{q}_y$.)

[34] Time series of the amplitude of the 2-day wave meridional wind are shown in Figure 6a at 30°N/S and 90 km (black curves). The amplitude is largest in July in the NH, with secondary peaks in January in the SH. Figure 6b shows time series of the zonal mean PV gradient in the region where the 2-day wave is generated. Negative PV gradients in the summer hemisphere are seen to coincide with periods of wave amplification, although the amplitude maximum in January is considerably weaker.

[35] *Norton and Thuburn* [1996, 1999] demonstrated that parameterized nonorographic GWD is necessary for the generation of a realistic 2-day wave in a GCM. The reason for this, they argue, is that GWD produces and maintains the wind shears that are necessary for generating the 2-day wave. Similar behavior occurs in the CMAM, as is demonstrated by the shaded curves in Figure 6a, which show results from the simulation without nonorographic GWD. (Note that the second year is repeated for easier comparison to the control simulation.) The amplitude maximum in July has now been reduced by a factor of four. Similar results are found at different locations.

[36] The 2-day wave amplitude in the control simulation (Figure 6a) exhibits a slower growth and decay than in the observations where it is more intermittent and is characterized by pulses of 20 to 30 day duration [*Fritts et al.*, 1999]. This behavior in the model is attributed to the fixed parameterized gravity wave source spectrum that is used. (Similar results are given by *Norton and Thuburn* [1999], where the 2-day wave was extracted with a narrower spectral window than was used here.) If a time-varying source spectrum were used, the shear zones could be made to vary more rapidly in time, causing a more intermittent 2-day wave.

[37] What is somewhat surprising is the lack of a strong 2-day wave in the control simulation in January, which nevertheless has a background state with large GWD-generated wind shears and negative PV gradients. This may be related to the position of the mesospheric easterly jet maximum, which occurs slightly higher in the SH (not shown). Consequently, stronger wave damping at these heights may be suppressing the growth of the wave. It may also be related to differences in the background winds, since relatively small changes can lead to large (factor of 2 to 3) differences in the 2-day wave amplitude [*Merzlyakov and Jacobi*, 2004].

5.2. Four-Day Wave

[38] The zonal wavenumber-frequency spectrum of EPFD averaged over southern high latitudes in the upper meso-

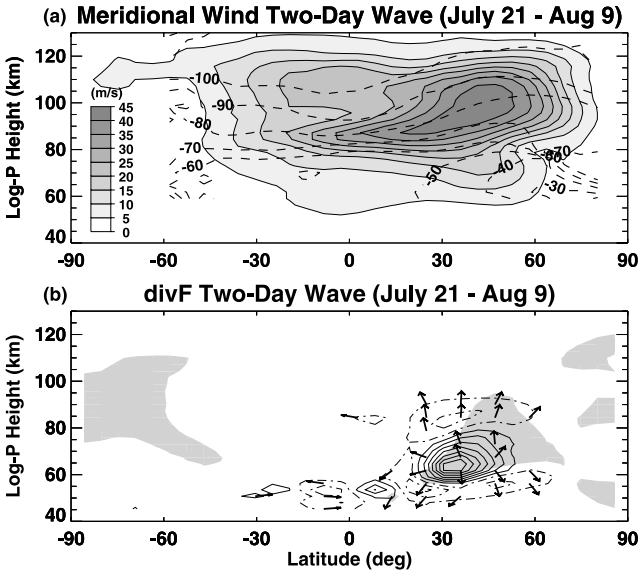

Figure 5. The 2-day wave ($m = -3$; $0.4 \le \omega \le 0.8$ cpd) computed from a 20-day period in July and August of the first year of the control simulation. (a) Amplitude (shaded) and phase (dashed lines; longitude of maximum in degrees) of the meridional wind component and (b) normalized EP flux vector ($\vec{F}$) and divergence ($\nabla \cdot \vec{F}$). Contour levels for $\nabla \cdot \vec{F}$ are staggered about zero using an interval of 10^{-4} kg m^{-1} s^{-2} (i.e., $\pm 0.5 \times 10^{-4}$, $\pm 1.5 \times 10^{-4}$, ...); negative values are dashed. The vertical component of $\vec{F}$ has been scaled by the aspect ratio of the plot. Shading in Figure 5b denotes regions where the latitudinal derivative of the zonal mean PV is negative. Note that the phase is computed for a single frequency ($\omega = 0.6$ cpd).

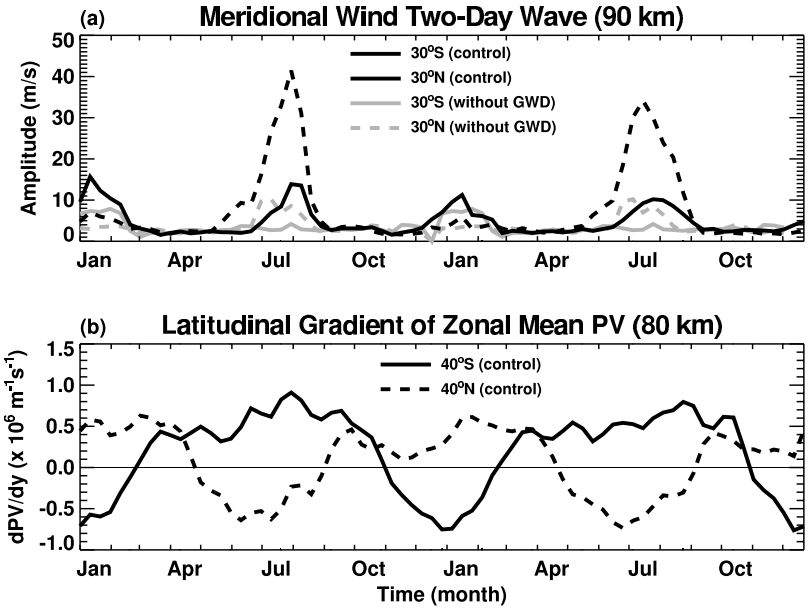

Figure 6. Time series of (a) the amplitude of the meridional wind component of the 2-day wave ($m = -3$; $0.4 \leq \omega \leq 0.8$ cpd) at 30°N/S, 90 km, and (b) the latitudinal derivative of the zonal mean PV at 40°N/S, 80 km. The black lines denote the control simulation; the shaded lines in Figure 6a are for the 1-year simulation without nonorographic GWD for which the second year is repeated. Results are computed using a 20-day window.

sphere for JJA is shown in Figure 7 for the control simulation. The spectrum is dominated by eastward traveling planetary waves $m = +1$ and 2. The broad spectral peak at $m = +1$ and $0.3 \leq \omega \leq 0.5$ cpd is the 4-day wave. Observations indicate that the frequency is generally closer to 0.25 cpd in the MLT [*Lawrence et al.*, 1995; *Palo et al.*, 1998]. This discrepancy is most likely due to differences between the simulated and observed basic states on which the wave propagates. Except for its frequency, all other characteristics of the wave (i.e., zonal wavenumber, horizontal propagation direction, and confinement to high latitudes) are similar to the observed 4-day wave.

[39] The amplitude and phase of the 4-day wave meridional wind is shown in Figure 8a for a 20-day period in July when the wave is strongest. The wave is confined to high latitudes, with the amplitude reaching 25 m/s near 90 km at 90°S; equatorward of 40°S the amplitude is negligible. Above 60 km the wave has an eastward phase tilt with increasing height. The temperature amplitude for the same time period (not shown) exhibits maxima of 7–9 K at 55 km and at 70 km near 70°S, with a rapid 180° phase shift in between, similar to observations [e.g., *Allen et al.*, 1997].

[40] Figure 8b shows the 4-day wave EP flux divergence and EP flux for the same 20-day period. The predominantly downward direction of the EP flux vectors indicates a strong downgradient (equatorward) heat flux in the SH polar mesosphere where the zonal mean temperature is decreasing equatorward from the warm winter pole (see Figure 3a of F02). This feature, as well as the dipole structure in $\nabla \cdot \vec{F}$, with positive values associated with the region of negative PV gradients, is characteristic of baroclinic instability.

[41] The temporal evolution of the 4-day wave meridional wind amplitude at 75°N/S and 90 km is shown in Figure 9a (black curves). The time series exhibit a strong hemispheric asymmetry during the winter months, with substantially larger amplitudes in the SH. This asymmetry is associated with the hemispheric asymmetry in the PV gradients (Figure 9b). Times when the wave is strong in SH winter coincide with large negative PV gradients. In the NH where there are no sustained periods of negative PV gradients, the

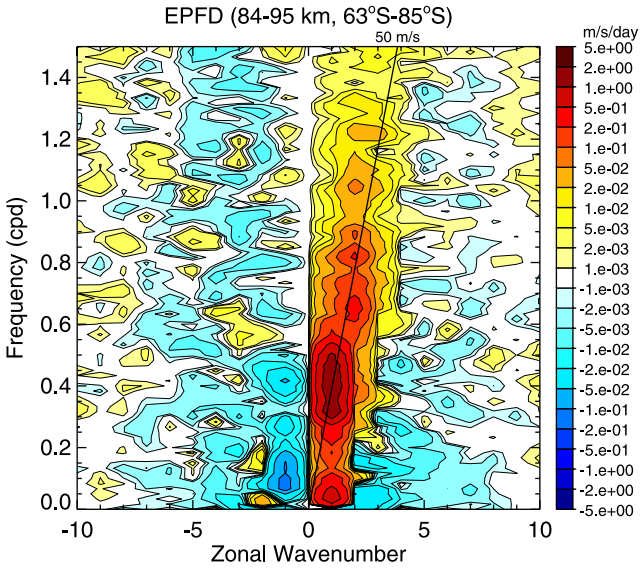

Figure 7. Zonal wavenumber (m) and frequency (ω) spectrum of $\nabla \cdot \vec{F}/(\rho_o\, a \cos\phi)$ averaged from 63°S to 85°S and from 84 to 95 km for June, July, and August of the control simulation. The broad spectral peak centered at $m = +1$ and $\omega \sim 0.4$ cpd is the 4-day wave. See Figure 4 caption for more details.

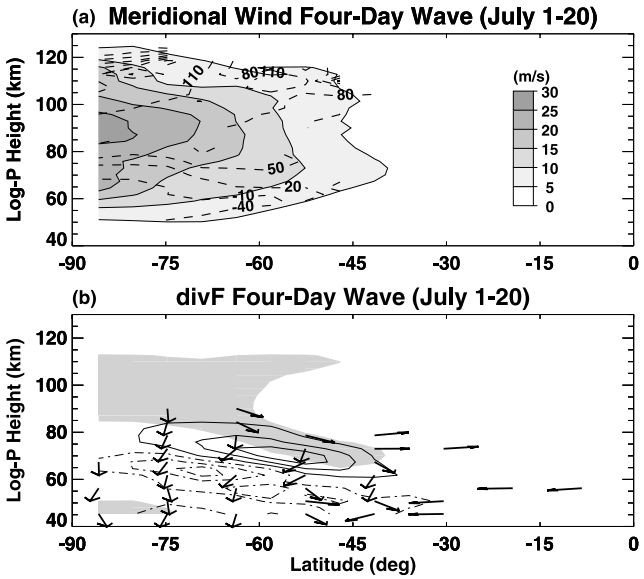

Figure 8. (a and b) Same as Figure 5 but for 4-day wave ($m = +1$; $0.2 \leq \omega \leq 0.5$ cpd) for the control simulation. Phase is computed for a single frequency ($\omega = 0.4$ cpd). Note that only the Southern Hemisphere is shown.

4-day wave amplitude is weak. Results at different locations in the polar mesosphere are similar to those shown in Figure 9.

[42] The hemispheric asymmetry in the negative PV gradients (and the corresponding hemispheric asymmetry in the 4-day wave amplitudes) is a direct consequence of the parameterized nonorographic GWD, as can be seen as follows. In NH winter, where the stratospheric westerlies are weaker than in SH winter (not shown), there is less filtering of the eastward traveling parameterized gravity waves. This results in less drag in the mesosphere, weaker wind shears, and the absence of sustained periods of negative PV gradients. This appears to be a robust result that does not depend upon the type of GWD parameterization used, only on the reasonable assumption that the gravity wave source spectrum contains both eastward and westward traveling waves. This suggests that the hemispheric asymmetry in the 4-day wave amplitude seen in the control simulation may occur in the real atmosphere. However, because of a lack of observations in the NH polar mesosphere, this conjecture cannot be verified at this time.

[43] The importance of the mesospheric wind reversals for the development of the 4-day wave is further underscored by the simulation without parameterized nonorographic GWD. The corresponding wave amplitudes (shaded curves in Figure 9a) are substantially weaker than for the control simulation. This behavior results from the absence of the wind reversals and negative PV gradients in the mesosphere (Figure 3a). The presence of nonorographic GWD therefore acts to maintain the strong shear zones that an unstable growing wave acts to weaken. If the GWD were suddenly turned off, the wave would quickly diminish, as described by *Norton and Thuburn* [1996] in the context of the 2-day wave.

[44] The 4-day wave in the stratosphere is largely insensitive to the presence of nonorographic GWD, as demonstrated in Figure 10, which shows time series of meridional wind amplitudes at 45 km. At this height, the wave is generated in the region of negative PV gradients on the poleward side of the stratospheric jet, which is present in both simulations (Figures 1a and 3a). Although the hemispheric asymmetry is less pronounced than at 90 km (Figure 9a), amplitudes in SH winter still exceed those in NH winter as

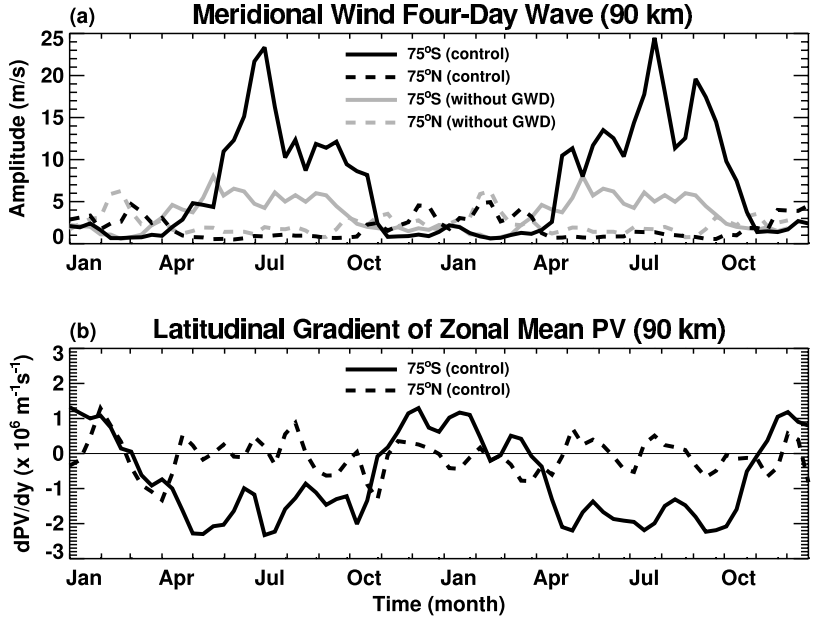

Figure 9. Time series of (a) the amplitude of the meridional wind component of the 4-day wave ($m = +1$; $0.2 \leq \omega \leq 0.5$ cpd) and (b) the latitudinal derivative of the zonal mean PV at 75°N/S, 90 km. The black lines denote the control simulation; the shaded lines in Figure 9a are for the 1-year simulation without nonorographic GWD for which the second year is repeated. Results are computed using a 20-day window.

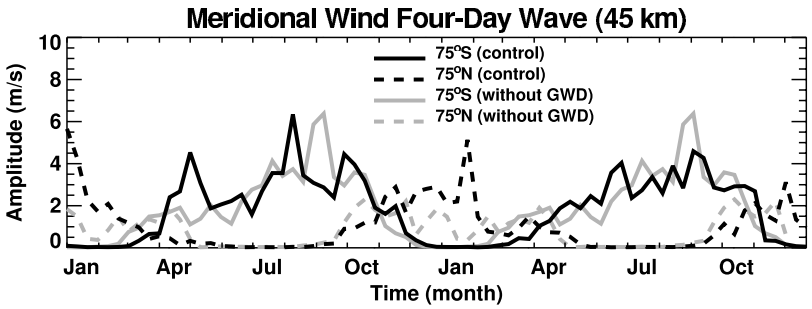

Figure 10. Same as Figure 9a but at 45 km.

in the observations [e.g., *Venne and Stanford*, 1982]. In both the model and the observations this asymmetry is a consequence of the stronger (and hence more unstable) winter westerlies in the SH.

[45] Previous studies [*Manney*, 1991; *Randel and Lait*, 1991; *Lawrence and Randel*, 1996] have suggested that barotropic instability associated with the "double-jet" structure in the CIRA zonal mean zonal winds is responsible for generating the 4-day wave in the mesosphere. Our results indicate that the barotropically unstable double-jet structure seen in the CIRA winds is not necessary for the development of a strong 4-day wave in the MLT. In the CMAM, strong vertical shears in the mean wind, which are produced by breaking gravity waves, render the zonal mean state baroclinically unstable, thus causing the wave to amplify.

5.3. Equatorial Waves

[46] Before discussing the resolved equatorial waves it is instructive to examine the zonal mean zonal winds since they play an important role in filtering the slower phase speed waves propagating upward from the troposphere. The corresponding monthly average time series of the tropical zonal winds for the control simulation are shown in Figure 11. The downward propagating signal between 40 and 90 km is the semiannual oscillation. It differs somewhat from observations [e.g., *Garcia et al.*, 1997], which have minimum wind speeds near 65 km and do not exhibit this uniform descent, which is due here to the parameterized nonorographic GWD. Observations also suggest a stronger first cycle of the year, which is not seen in the simulation.

[47] Figure 12 shows the zonal wavenumber-frequency spectrum of the annual mean EPFD averaged over the tropical upper mesosphere. With the exception of several positive (i.e., yellow) regions for $m < 0$, all of the disturbances are upward propagating. This follows from the fact that upward propagating eastward (westward) traveling equatorial waves undergoing dissipation have negative (positive) vertical EP flux and a corresponding positive (negative) EPFD. The preponderance of eastward traveling waves is presumably a consequence of the westward mean winds between 75 and 95 km and below 40 km (Figure 11), which filter out most of the westward traveling waves with phase speeds less than 50 m/s.

[48] The spectral peaks at $m = -1$, $\omega = 1$ and $m = -2$, $\omega = 2$ in Figure 12 are the migrating diurnal and semidiurnal

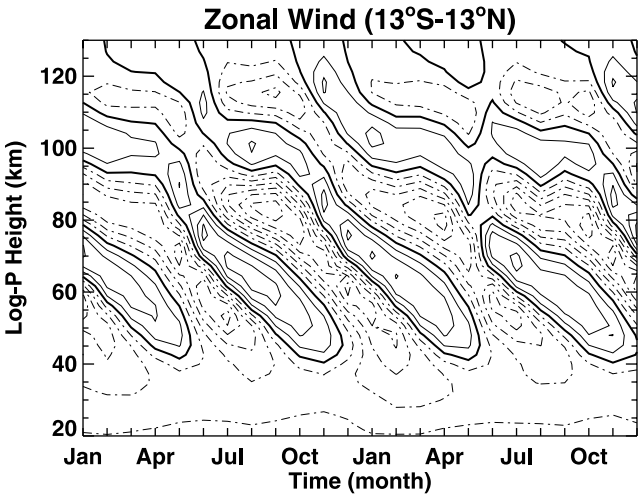

Figure 11. Monthly averaged zonal mean zonal wind averaged from 13°S to 13°N for the control simulation. A contour interval of 10 m/s is used. Easterlies are dashed; the zero contour is thick.

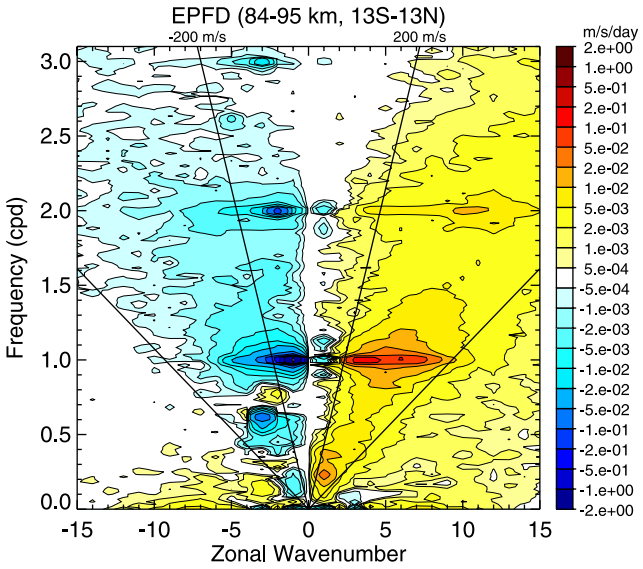

Figure 12. Annual mean zonal wavenumber (m) and frequency (ω) spectrum of $\nabla \cdot \vec{F}/(\rho_o\, a \cos\phi)$ averaged from 13°S to 13°N and from 84 to 95 km for the control simulation. The spectral peak at $m = -1$ and $\omega = 1$ cpd is the migrating diurnal tide; $|m| < 8$ ($m \neq -1$) and $\omega = 1$ cpd are nonmigrating diurnal tides. The two unlabeled diagonal lines denote the plus and minus 50 m/s phase speeds. See Figure 4 caption for more details.

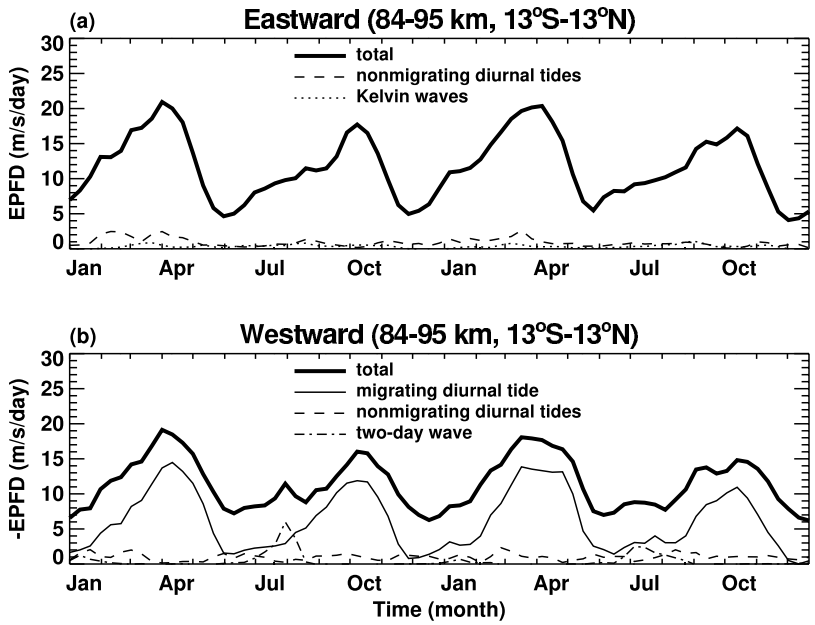

Figure 13. Time series of $\nabla \cdot \vec{F}/(\rho_o\, a \cos\phi)$ averaged from 13°S to 13°N and from 84 to 95 km for the control simulation: (a) eastward and (b) westward traveling disturbances. The wave types are defined as nonmigrating diurnal tides ($|m| = 1-5$ ($m \neq -1$), $\omega = 1$ cpd), migrating diurnal tide ($m = -1$, $\omega = 1$ cpd), Kelvin waves ($m = +1-5$, $\omega \leq 0.3$ cpd), and 2-day wave ($m = -3$, $0.4 \leq \omega \leq 0.8$ cpd). The thick solid lines denote the sum of all wavenumbers and frequencies for each direction. Results are computed using a 20-day window.

tides, respectively. The migrating diurnal tide is seen to be the largest single contributor to the total wave forcing. Of the nonmigrating tides, eastward traveling diurnal frequencies with $m < 8$ are strongest; most of these are forced by the deep convective parameterization, as discussed by *Horinouchi et al.* [2003]. Preliminary analysis shows that the nonmigrating diurnal tides in the control simulation are in reasonable agreement with TIDI (TIMED Doppler Interferometer on board the TIMED satellite) wind observations in the MLT between 40°N and 40°S (J. Oberheide, personal communication, 2005).

[49] Time series of EPFD averaged over the tropical upper mesosphere (85 to 95 km) for both eastward and westward traveling waves are shown in Figure 13. The EPFD for the sum of all westward traveling waves (Figure 13b) is dominated by the migrating diurnal tide, with maxima of nearly −15 m/s/day near the equinoxes when the diurnal tide is strongest. These values are consistent with the observed estimates of tidal forcing of *Lieberman and Hays* [1994]. Despite this strong tidal forcing, the observed westward wind maximum near 100 km [*Lieberman and Hays*, 1994] is absent in the simulation (Figure 11). The reason for this is the compensating positive forcing from eastward propagating disturbances (Figure 13a). However, because of a lack of observations, it is not known whether this positive forcing is realistic or not. It is conceivable that the model has underestimated westward propagating inertia-gravity waves in the MLT, perhaps through critical-level filtering as noted earlier. A stronger westward propagating gravity-wave spectrum could then balance the forcing from the eastward waves, leaving a net westward forcing from the migrating diurnal tide, resulting in westward zonal mean zonal winds at 100 km.

[50] The 2-day wave provides forcing of up to −5 m/s/day in July (Figure 13b) when the wave is strongest (Figure 6a). The relative importance of the 2-day wave is somewhat stronger lower down in the 75 to 85 km region (not shown), where it provides forcing in July of nearly the same strength as the migrating diurnal tide in equinox. The 2-day wave forcing is consistent with the WACCM results discussed by *Richter and Garcia* [2006], with the exception that their results show stronger forcing in January, which is not seen in the CMAM on account of the weak 2-day wave at this time of year.

[51] The EPFD from both eastward and westward traveling nonmigrating diurnal tides provide only a small amount of wave forcing in each direction (Figure 13). In the 95 to 105 km region (not shown), the contribution from the eastward traveling diurnal tides is slightly larger, but still less than about 5 m/s/day. Figure 13a also shows that planetary-scale Kelvin waves have a negligible impact. This is in agreement with the results of *Horinouchi et al.* [2003], which show that the vertical component of the EP flux due to planetary Kelvin waves is less than 10% of the total for all eastward traveling disturbances in most GCMs (including the CMAM), despite there being a significant Kelvin wave response in kinetic energy in the stratosphere. Most of the forcing from eastward traveling disturbances therefore comes from the broad spectrum of inertia gravity waves seen in Figure 12.

[52] The total forcing for both the eastward and westward traveling waves (thick curves in Figure 13) exhibits semiannual variations of similar magnitude, with maxima occurring near the equinoxes. The semiannual variation for the westward waves results primarily from the semiannual variation of the migrating diurnal tide, whose causes are

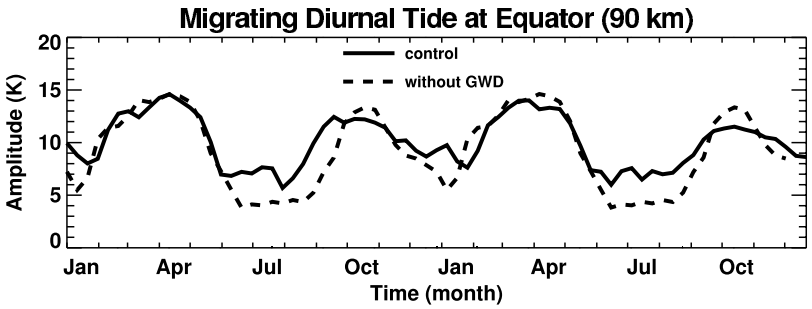

Figure 14. Temperature amplitude of the migrating diurnal tide ($m = -1$, $\omega = 1$ cpd) at the equator and 90 km for the control simulation and the simulation without nonorographic GWD (second year is repeated). Results are computed using a 20-day window.

understood in the CMAM [*McLandress*, 2002a, 2002b]. The semiannual variation for the eastward waves results primarily from the removal of the slower phase speed waves by critical levels in the lower mesosphere in the solstice months and to a lesser extent from the increase in EPFD for high phase speed waves having frequencies near 1.0 and 0.5 cpd in April. The latter is due to an increase in tropospheric deep convective latent heating, which has been discussed by *McLandress* [1997] in the context of the migrating diurnal tide. The former is due to the presence of strong vertical shears in the zonal mean zonal wind in the 55–70 km region (Figure 11), which result from the parameterized GWD as discussed earlier.

[53] Several studies have suggested that nonlinear interactions between the 2-day wave and the migrating diurnal tide are responsible for the observed semiannual variation of the tide in the tropical MLT, with a strong 2-day wave at solstice sapping energy from the tide, causing it to weaken [*Norton and Thuburn*, 1999; *Palo et al.*, 1999]. This effect, if it occurs at all, appears to be very weak in the CMAM, as is demonstrated in Figure 14, which shows the amplitude of the migrating diurnal tide temperature in the upper mesosphere at the equator. Both simulations exhibit a strong semiannual tidal variation, in spite of the fact that the simulation without nonorographic GWD has a very weak 2-day wave (Figure 6a). Moreover, the tidal amplitude in July for the control simulation, which has a strong 2-day wave at this time, is somewhat larger. As discussed by *McLandress* [2002a, 2002b], seasonal variations of the mean zonal winds and tropospheric heating are responsible for the semiannual variation of the tide in the CMAM.

6. Gradient Wind Balance

[54] The starting point for the discussion on gradient wind balance in the MLT is the zonal mean meridional wind equation in log-pressure coordinates [*Andrews et al.*, 1987], rearranged as follows:

$$\bar{u}\left(f + \frac{\bar{u}\tan\phi}{a}\right) + \frac{1}{a}\frac{\partial\bar{\Phi}}{\partial\phi} = \bar{F}_v - \frac{1}{a\cos\phi}\frac{\partial}{\partial\phi}\left(\overline{v'v'}\cos\phi\right) - \frac{1}{\rho_o}\frac{\partial}{\partial z}\left(\rho_o\overline{v'w'}\right) - \overline{u'u'}\,\frac{\tan\phi}{a} \quad (2)$$

where $\bar{F}_v$ includes the time tendency, the meridional and vertical zonal mean advection, and the parameterized forcing and dissipation terms. The last three terms on the right hand side of (2) are the Reynolds stress terms.

[55] The terms on the left hand side of (2) comprise the three terms in the gradient wind equation; their sum will be referred to as the gradient wind residual. The gradient wind is computed from the zonal mean geopotential after setting the residual to zero. At the two grid points adjacent to the equator l'Hôpital's rule is used; elsewhere the solution of the quadratic equation for the gradient wind is employed (see *Fleming et al.* [1990] for details) This is the procedure used in generating the CIRA zonal mean zonal winds [*Fleming et al.*, 1990].

[56] Figure 15 shows the gradient winds for JJA and MAM and the corresponding differences with the true zonal mean zonal winds shown in Figure 1. In the extratropics below about 80 km the agreement is very good. However, above this region in the extratropical MLT, the gradient wind approximation underestimates the wind reversals. This effect is more pronounced in JJA in the summer hemisphere where the gradient wind reversal is weaker by up to 40%, in agreement with satellite wind and temperature observations [*Lieberman*, 1999a]. Above 130 km, the gradient wind approximation fails on account of strong ion drag and molecular diffusion. The approximation also breaks down at low latitudes where the Coriolis force is weak. This becomes more pronounced in the MLT, especially in MAM where the gradient winds exhibit an anomalous region of strong westerlies centered at 100 km, which, incidentally, is also evident in the CIRA winds at these months.

[57] Figures 16a and 16b show the gradient wind residual for JJA and MAM. Equatorward of about 30°, the largest imbalance (with magnitudes of up to 100 m/s/day) occurs in MAM. *Miyahara et al.*'s [2000] conclusion that this is a result of the migrating diurnal tide was based on the assumption that the migrating diurnal tide was the dominant disturbance in their model in this region. However, the presence of other disturbances, such as nonmigrating tides, may also be playing a significant role. To clarify this, the Reynolds stress is computed using only the migrating diurnal tide winds. These results, which are shown in Figures 16c and 16d indicate that equatorward of 30° the tide is responsible for nearly all of the imbalance. The fact that the tidal Reynolds stress is largest at equinox when the tide is strongest also explains why the agreement between the gradient wind and the actual wind in the tropical MLT is worse in MAM than it is in JJA. The seasonal variation of the

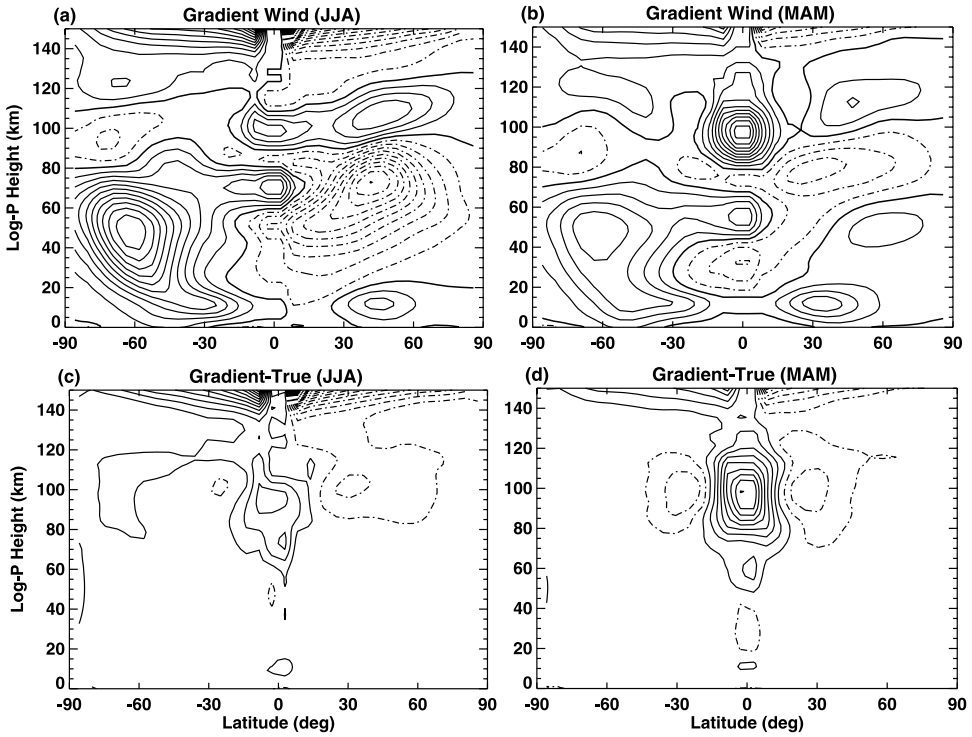

Figure 15. (a and b) Gradient winds and (c and d) differences between gradient and true zonal winds for June, July, and August (Figures 15a and 15c) and March, April, and May (Figures 15b and 15d). Contour levels are 0, ±10, ±20, etc., with easterlies dashed (Figures 15a and 15b), and ±5, ±15, ±25, etc., with negative differences dashed (Figures 15c and 15d). The true zonal winds are shown in Figure 1.

tidal Reynolds stress, which is shown in Figure 17b at 100 km, indicates that the tide accounts for most of the imbalance at low latitudes at all months, as seen by comparing it to the gradient wind residual shown in Figure 17a.

[58] Figure 16 indicates that poleward of 30° disturbances other than the migrating diurnal tide produce most of the imbalance. This is also seen in Figure 17c, which shows time series of the Reynolds stress for the nontidal disturbances. The stress term maximizes in the summer hemispheres between 30° and 60°, with a secondary maximum in SH winter at high latitudes that is most likely related to the 4-day wave. Figure 17d shows the zonal mean meridional wind component of the parameterized nonorographic GWD. It is somewhat weaker than the resolved nontidal forcing (Figure 17c) and peaks at middle to high latitudes in the summer hemisphere. This results from the filtering of the meridionally propagating parameterized gravity waves by the zonal mean meridional wind, which is strongest in the summer hemisphere mesosphere (Figure 1c). Figures 17c and 17d indicate that the gradient wind underestimation of the true zonal wind reversal in the extratropical MLT (negative values seen in Figure 15c) is due to a combination of both resolved and parameterized waves, since the absence of either one of these terms would result in closer agreement between the gradient and true winds.

7. Conclusions

[59] The extended Canadian Middle Atmosphere Model has been used to examine the large-scale dynamics of the mesosphere and lower thermosphere (MLT). Attention is focused on the region below about 120 km where the physical processes in the model are most representative. The primary focus of the study is on planetary waves, and their impact on the zonal mean zonal and meridional momentum budgets. These include the 2-day and 4-day waves, which are generated in the extratropical upper mesosphere during the solstice months, and equatorial waves, which are forced primarily in the troposphere and propagate up to the MLT. The latter include migrating and nonmigrating diurnal tides, Kelvin waves and inertia gravity waves. To elucidate the role of mean wind shears on the 2-day and 4-day waves, simulations with and without parameterized nonorographic gravity wave drag (GWD) are examined.

[60] In agreement with the modeling studies of *Norton and Thuburn* [1996, 1999], the amplification of the 2-day wave in the model is closely linked to the presence of strong shears in the zonal mean zonal winds that are brought about by the parameterized GWD. Although the wave amplitude is quite realistic in July, it is too weak in January despite there being strong shears at that time. While the reason for the weak 2-day wave in January is presently unclear, it does suggest that the relationship between GWD-induced wind shears and the 2-day wave is not as straightforward as originally thought.

[61] Concerning the 4-day wave, which up to now has not been studied in detail using middle atmosphere general circulation models, we have demonstrated that parameterized nonorographic GWD plays an important role in its generation in the MLT. The fact that the simulated 4-day

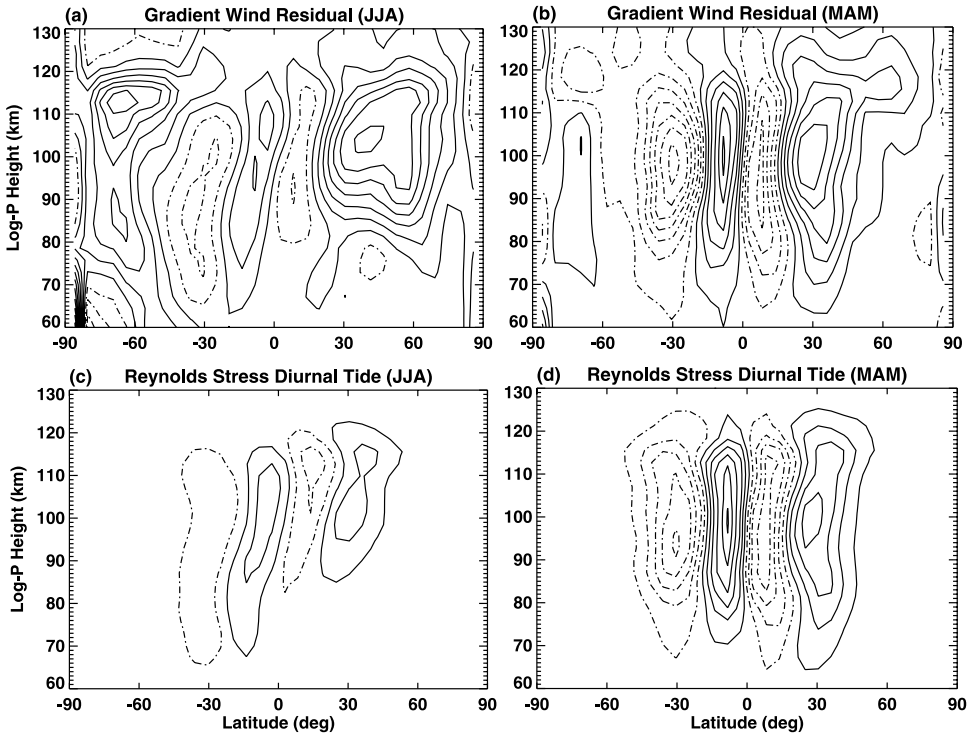

Figure 16. Gradient wind residual for (a) June, July, and August and (b) March, April, and May for the control simulation. (c and d) Corresponding Reynolds stress terms computed using only the migrating diurnal tide. Contour levels are staggered about zero using an interval of 20 m/s/day (i.e., ±10, ±30, . . .); negative values are dashed.

wave is considerably stronger in the MLT in southern polar winter than in northern polar winter is attributed to the stronger wind shears in the upper mesosphere in SH winter. These shears are associated with the reversal of the zonal mean zonal winds which arise from the parameterized GWD. In NH winter, the shears are much weaker because of weaker GWD which results from reduced filtering of the parameterized gravity waves by the weaker stratospheric westerlies. The importance of wind shears in generating the 4-day wave is further underscored by the fact that the wave amplitude in the MLT was much weaker in the simulation without nonorographic GWD.

[62] Previous studies [*Manney*, 1991; *Randel and Lait*, 1991; *Lawrence and Randel*, 1996] have suggested that barotropic instability associated with the "double-jet" structure in the CIRA zonal mean zonal winds is responsible for generating the 4-day wave in the mesosphere. While this is a plausible physical mechanism, it is unclear just how representative this jet structure is, since it was based on only a few years of satellite data that extended up to 80 km [*Fleming et al.*, 1990]. In our simulation with nonorographic GWD, it is baroclinic instability arising from strong vertical shears in the mean winds that is responsible for the amplification of the 4-day wave in the MLT.

[63] The sensitivity of our results to the GWD parameterization, in particular the source spectrum, would seem to be fairly small. The hemispheric asymmetry in the filtering of the parameterized gravity waves that is needed to bring about stronger vertical shears in SH winter than in NH winter appears to be a robust result that other models could produce. The only assumption is that the parameterized source spectrum contains both eastward and westward traveling gravity waves.

[64] The role of equatorial wave forcing of the zonal mean zonal wind in the 85 to 95 km region has also been investigated. The migrating diurnal tide is found to provide most of the forcing for the resolved westward traveling disturbances. The magnitude of the tidal forcing and its semiannual variation, with strongest forcing in equinoxes when the tide is strongest, is in agreement with observations [*Lieberman and Hays*, 1994]. To a large extent the forcing from westward traveling waves is compensated by forcing from eastward traveling waves, which are made up of smaller-scale waves, namely inertia gravity waves. The 2-day wave provides about one half of the total westward wave drag in July. Other planetary-scale waves, in particular nonmigrating tides and Kelvin waves, were found to provide only weak forcing in the upper mesosphere.

[65] While the results in the tropics depend to some extent on the convective parameterization used in the CMAM, they do shed some light on the role of tides and other resolved waves in driving the zonal winds. Some of these results will be model-dependent, particularly the nonmigrating diurnal tides which are forced to a large extent by the convective parameterization. Therefore it is likely that different models would produce different resolved wave spectra in the MLT. However, because of a lack of observations of convectively generated equatorial waves in the lower stratosphere, it is not possible at present to say which parameterization is more correct in this respect. The migrating diurnal tide results, however, are not strongly

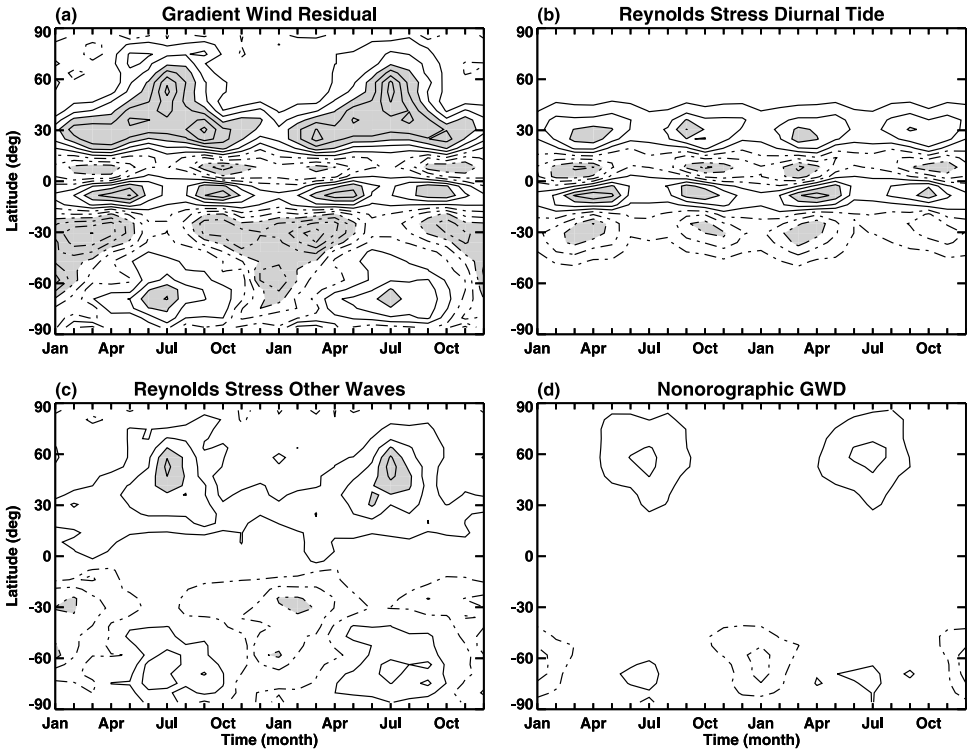

Figure 17. Monthly mean time series of terms in the zonal mean meridional wind equation at 100 km for the control simulation: (a) gradient wind residual, (b) Reynolds stress terms computed using only the migrating diurnal tide, (c) Reynolds stress terms computed using all other disturbances (i.e., excluding the migrating diurnal tide), and (d) nonorographic GWD. Contours are staggered about zero using an interval of 30 m/s/day (i.e., ±15, ±45, . . .); negative values are dashed. Shading is used for magnitudes exceeding 75 m/s/day.

dependent on the convective parameterization since solar heating is the dominant forcing mechanism.

[66] Finally, we have expanded on the numerical study of *Miyahara et al.* [2000] by explicitly demonstrating that it is the migrating diurnal tide that is responsible for the gradient wind imbalance in the equatorial MLT, especially at equinox when the tide is strongest. Other resolved waves, as well as parameterized gravity waves, were found to be important at middle and high latitudes during solstice. These results shed some light on the observational study of *Lieberman* [1999a], which suggested that departures from gradient wind balance in the extratropical MLT could arise from mean advection by the meridional circulation and drag from meridionally propagating gravity waves. Our results indicate that mean advection plays an insignificant role and that both resolved waves and parameterized gravity waves are largely responsible for the imbalance in the summer hemisphere at middle and high latitudes.

[67] **Acknowledgments.** The authors would like to thank the three anonymous reviewers for helpful suggestions and comments. C.M. thanks Dave Ortland for providing IDL code for the spherical harmonic transforms. This work has been supported through the "Modelling of Global Chemistry for Climate" Project, which is funded by the Natural Sciences and Engineering Research Council of Canada, the Canadian Foundation for Climate and Atmospheric Sciences, and the Canadian Space Agency.

References

Allen, D. R., J. L. Stanford, L. S. Elson, E. F. Fishbein, L. Froidevaux, and J. W. Waters (1997), The 4-day wave as observed from the Upper Atmosphere Research Satellite Microwave Limb Sounder, *J. Atmos. Sci.*, *54*, 420–434.

Andrews, D. G., J. R. Holton, and C. B. Leovy (1987), *Middle Atmosphere Dynamics*, 489 pp., Elsevier, New York.

Beagley, S. R., J. de Grandpré, J. N. Koshyk, N. A. McFarlane, and T. G. Shepherd (1997), Radiative-dynamical climatology of the first-generation Canadian Middle Atmosphere Model, *Atmos. Ocean*, *35*, 293–331.

Fleming, E. L., and S. Chandra (1989), Equatorial zonal wind in the middle atmosphere derived from geopotential height and temperature data, *J. Atmos. Sci.*, *46*, 860–866.

Fleming, E. L., S. Chandra, J. J. Barnett, and M. Corney (1990), Zonal mean temperature, pressure, zonal wind and geopotential height as functions of latitude, *Adv. Space Res.*, *10*(12), 11–59.

Fomichev, V. I., W. E. Ward, S. R. Beagley, C. McLandress, J. C. McConnell, N. A. McFarlane, and T. G. Shepherd (2002), Extended Canadian Middle Atmosphere Model: Zonal-mean climatology and physical parameterizations, *J. Geophys. Res.*, *107*(D10), 4087, doi:10.1029/2001JD000479.

Fraser, G. J., G. Hernandez, and R. W. Smith (1993), Eastward-moving 2–4 day waves in the winter antarctic mesosphere, *Geophys. Res. Lett.*, *20*, 1547–1550.

Fritts, D. C., J. R. Isler, R. S. Lieberman, M. D. Burrage, D. R. Marsh, T. Nakamura, T. Tsuda, R. A. Vincent, and I. M. Reid (1999), Two-day wave structure and mean flow interactions observed by radar and High Resolution Doppler Imager, *J. Geophys. Res.*, *104*, 3953–3969.

Garcia, R. G., and R. T. Clancy (1990), Seasonal variation in equatorial mesospheric temperatures observed by SME, *J. Atmos. Sci.*, *47*, 1666–1673.

Garcia, R. G., T. J. Dunkerton, R. S. Lieberman, and R. A. Vincent (1997), Climatology of the semiannual oscillation of the tropical middle atmosphere, *J. Geophys. Res.*, *102*, 26,019–26,032.

Hays, P. B., et al. (1994), Observations of the diurnal tide from space, *J. Atmos. Sci.*, *51*, 3077–3093.

Hines, C. O. (1997a), Doppler–spread parameterization of gravity-wave momentum deposition in the middle atmosphere. Part 1: Basic formulation, *J. Atmos. Sol. Terr. Phys.*, *59*, 371–386.

Hines, C. O. (1997b), Doppler-spread parameterization of gravity-wave momentum deposition in the middle atmosphere. Part 2: Broad and quasi-monochromatic spectra, and implementation, *J. Atmos. Sol. Terr. Phys.*, *59*, 387–400.

Horinouchi, T., et al. (2003), Tropical cumulus convection and upward-propagating waves in middle-atmosphere GCMs, *J. Atmos. Sci.*, *60*, 2765–2782.

Lawrence, B. N., and W. J. Randel (1996), Variability in the mesosphere observed by the Nimbus 6 pressure modulator radiometer, *J. Geophys. Res.*, *101*, 23,475–23,489.

Lawrence, B. N., G. J. Fraser, R. A. Vincent, and A. Phillips (1995), The 4-day wave in the Antarctic mesosphere, *J. Geophys. Res.*, *100*, 18,899–18,908.

Lieberman, R. S. (1999a), The gradient wind in the mesosphere and lower thermosphere, *Earth Planets Space*, *51*, 751–761.

Lieberman, R. S. (1999b), Eliassen-Palm fluxes of the 2-day wave, *J. Atmos. Sci.*, *56*, 2846–2861.

Lieberman, R. S. (2002), Corrigendum, *J. Atmos. Sci.*, *59*, 2625–2627.

Lieberman, R. S., and P. B. Hays (1994), An estimate of the momentum deposition in the lower thermosphere by the observed diurnal tide, *J. Atmos. Sci.*, *51*, 3094–3105.

Limpasuvan, V., D. L. Wu, M. J. Schwartz, J. W. Waters, Q. Wu, and T. L. Killeen (2005), The two-day wave in EOS MLS temperature and wind measurements during 2004–2005 winter, *Geophys. Res. Lett.*, *32*, L17809, doi:10.1029/2005GL023396.

Manney, G. L. (1991), The stratospheric 4-day wave in NMC data, *J. Atmos. Sci.*, *48*, 1798–1811.

Manson, A. H., et al. (2002), Gravity wave activity and dynamical effects in the middle atmosphere (60–90 km): Observations from an MF/MLT radar network, and results from the Canadian Middle Atmosphere Model (CMAM), *J. Atmos. Sol. Terr. Phys.*, *64*, 65–90.

McLandress, C. (2002a), The seasonal variation of the propagating diurnal tide in the mesosphere and lower thermosphere. Part I: The role of gravity waves and planetary waves, *J. Atmos. Sci.*, *59*, 893–906.

McLandress, C. (2002b), The seasonal variation of the propagating diurnal tide in the mesosphere and lower thermosphere. Part II: The role of tidal heating and zonal mean winds, *J. Atmos. Sci.*, *59*, 907–922.

McLandress, C. (1997), Seasonal variability of the diurnal tide: Results from the Canadian middle atmosphere general circulation model, *J. Geophys. Res.*, *102*, 29,747–29,764.

McLandress, C., and J. F. Scinocca (2005), The GCM response to current parameterizations of nonorographic gravity wave drag, *J. Atmos. Sci.*, *62*, 2394–2413.

McLandress, C., G. G. Shepherd, and B. H. Solheim (1996), Satellite observations of thermospheric tides: Results from the Wind Imaging Interferometer on UARS, *J. Geophys. Res.*, *101*, 4093–4114.

Merzlyakov, E. G., and C. Jacobi (2004), Quasi-two-day wave in an unstable summer atmosphere—Some numerical results on excitation and propagation, *Ann. Geophys.*, *22*, 1917–1929.

Miyahara, S. (1978), Zonal mean winds induced by vertically propagating atmospheric tidal waves in the lower thermosphere, *J. Meteorol. Soc. Jpn.*, *56*, 548–558.

Miyahara, S., Y. Yoshida, and Y. Miyoshi (1993), Dynamic coupling between the lower and upper atmosphere by tides and gravity waves, *J. Atmos. Terr. Phys*, *55*, 1039–1053.

Miyahara, S., D. Yamamoto, and Y. Miyoshi (2000), On the geostrophic balance of mean zonal winds in the mesosphere and lower thermosphere, *J. Meteorol. Soc. Jpn.*, *78*, 683–688.

Norton, W. A., and J. Thuburn (1996), The two-day wave in a middle atmosphere GCM, *Geophys. Res. Lett.*, *23*, 2113–2116.

Norton, W. A., and J. Thuburn (1997), The mesosphere in the extended UGAMP GCM, in *Gravity Wave Processes and Their Parameterization in Global Climate Models*, edited by K. Hamilton, pp. 383–401, Springer, New York.

Norton, W. A., and J. Thuburn (1999), Sensitivity of mesospheric mean flow, planetary waves, and tides to strength of gravity wave drag, *J. Geophys. Res.*, *104*, 30,897–30,911.

Palo, S. E., Y. I. Portnyagin, J. M. Forbes, N. A. Makarov, and E. G. Merzlyakov (1998), Transient eastward-propagating long-period waves observed over the South Pole, *Ann. Geophys.*, *16*, 1486–1500.

Palo, S. E., R. G. Roble, and M. E. Hagan (1999), Middle atmosphere effects of the quasi-two-day wave determined from a general circulation model, *Earth Planets Space*, *51*, 629–647.

Randel, W. J., and L. R. Lait (1991), Dynamics of the 4-day wave in the Southern Hemisphere polar stratosphere, *J. Atmos. Sci.*, *48*, 2496–2508.

Richter, J. H., and R. R. Garcia (2006), On the forcing of the Mesospheric Semi-Annual Oscillation in the Whole Atmosphere Community Climate Model, *Geophys. Res. Lett.*, *33*, L01806, doi:10.1029/2005GL024378.

Riggin, D. M., R. S. Lieberman, R. A. Vincent, A. H. Manson, C. E. Meek, T. Nakamura, T. Tsuda, and Y. I. Portnyagin (2004), The 2-day wave during the boreal summer of 1994, *J. Geophys. Res.*, *109*, D08110, doi:10.1029/2003JD004493.

Schmidt, H., G. P. Brasseur, M. Charron, E. Manzini, M. A. Giorgetta, T. Diehl, V. I. Fomichev, D. Kinnison, D. Marsh, and S. Walters (2006), The HAMMONIA Chemistry Climate Model: Sensitivity of the mesopause region to the 11-year solar cycle and CO_2 doubling, *J. Clim.*, in press.

Scinocca, J. F., and N. A. McFarlane (2004), The variability of modeled tropical precipitation, *J. Atmos. Sci.*, *61*, 1993–2015.

Swinbank, R., and D. A. Ortland (2003), Compilation of wind data for the Upper Atmosphere Research Satellite (UARS) Reference Atmosphere Project, *J. Geophys. Res.*, *108*(D19), 4615, doi:10.1029/2002JD003135.

Venne, D. E., and J. L. Stanford (1982), An observational study of high-latitude stratospheric planetary waves in winter, *J. Atmos. Sci.*, *39*, 1026–1034.

Wu, D. L., P. B. Hays, W. R. Skinner, A. R. Marshall, M. D. Burrage, R. S. Lieberman, and D. A. Ortland (1993), Observations of the quasi 2-day wave from the High-Resolution Doppler Imager on UARS, *Geophys. Res. Lett.*, *20*, 2853–2856.

Zhang, G. J., and N. A. McFarlane (1995), Sensitivity of climate simulations to the parameterization of cumulus convection in the Canadian Climate Center General-Circulation Model, *Atmos. Ocean*, *33*, 407–446.

S. R. Beagley, V. I. Fomichev, and K. Semeniuk, Department of Earth and Space Science and Engineering, York University, 4700 Keele Street, Toronto, ON, Canada M3J 1P3. (beagley@nimbus.yorku.ca; victor@nimbus.yorku.ca; kirill@nimbus.yorku.ca)

N. A. McFarlane, SPARC IPO, Department of Physics, University of Toronto, 60 St. George Street, Toronto, ON, Canada M5S 1A7. (norm.mcfarlane@ec.gc.ca)

C. McLandress and T. G. Shepherd, Department of Physics, University of Toronto, 60 St. George Street, Toronto, ON, Canada M5S 1A7. (charles@atmosp.physics.utoronto.ca; tgs@atmosp.physics.utoronto.ca)

W. E. Ward, Department of Physics, University of New Brunswick, P.O. Box 4400, Fredericton, NB, Canada E3B 5A3. (wward@unb.ca)